

Towards Predicting Fine Finger Motions from Ultrasound Images via Kinematic Representation

Dean Zadok*, Oren Salzman*, Alon Wolf[†] and Alex M. Bronstein*

*Department of Computer Science, Technion, Haifa, Israel

Email: {deanzadok,osalzman,bron}@cs.technion.ac.il

[†]Department of Mechanical Engineering, Technion, Haifa, Israel

Email: alonw@me.technion.ac.il

Abstract—A central challenge in building robotic prostheses is the creation of a sensor-based system able to read physiological signals from the lower limb and instruct a robotic hand to perform various tasks. Existing systems typically perform discrete gestures such as pointing or grasping, by employing electromyography (EMG) or ultrasound (US) technologies to analyze the state of the muscles. In this work, we study the inference problem of identifying the activation of specific fingers from a sequence of US images when performing dexterous tasks such as keyboard typing or playing the piano. While estimating finger gestures has been done in the past by detecting prominent gestures, we are interested in classification done in the context of fine motions that evolve over time. We consider this task as an important step towards higher adoption rates of robotic prostheses among arm amputees, as it has the potential to dramatically increase functionality in performing daily tasks. Our key observation, motivating this work, is that modeling the hand as a robotic manipulator allows to encode an intermediate representation wherein US images are mapped to said configurations. Given a sequence of such learned configurations, coupled with a neural-network architecture that exploits temporal coherence, we are able to infer fine finger motions. We evaluated our method by collecting data from a group of subjects and demonstrating how our framework can be used to replay music played or text typed. To the best of our knowledge, this is the first study demonstrating these downstream tasks within an end-to-end system.

I. INTRODUCTION

Bionic hands or robotic prostheses were sought after for decades yet the first commercially-available robotic prostheses only became available in 2007 [3] and a fully-functioning prosthesis enabling all the range of daily tasks is still out of reach. Existing robotic prostheses are typically connected to the limb of an amputee (or to a subject with severe phalanx or palm deformations) when the subject’s muscles still respond to electric potentials generated by the brain [11]. These electric potentials allow inferring different finger motions by placing a non-invasive sensor on the residual limb, having subjects attempt these motions or gestures, and then discriminating between the different types of electric potentials that are generated through the arm muscles [7, 23]. This sensing technology, called electromyography (EMG), allows the reproduction of grasp flexion and extension yet is unable to reproduce finer motions typically involved in daily tasks.

Recently, it was shown that replacing EMG with ultrasound (US) imaging that captures the muscles’ morphological state

allows to better differentiate between discrete gestures or to classify full-finger flexion [6]. These images are obtained by placing an US probe on the residual limb and its efficacy is based on the fact that the muscles generate different deformation patterns for different actions, and this behavior can be generalized among different subjects [6, 34, 35, 36].

Arguably, the most popular approach to infer motions from (high-dimensional) US images is via data-driven methods [19, 34, 36]. However, to the best of our knowledge, these methods still fall short of fully predicting dexterous hand motions or fine finger motions that a subject intended to perform. Predicting such motions, which is the focus of our work, is instrumental to the fine control of robotic hands and, consequently, to increase adoption rates of robotic prostheses.

Specifically, the key question this research aims to answer is *To what extent can we predict and differentiate between fine finger motions by only having access to a stream of US images of the lower-arm muscles?* As for running examples, we consider the tasks of piano playing and keyboard typing. In these tasks, the finger gestures required to press or type or usually more fine than those required to grasp objects or fully flex the fingers, generating smaller and less observable lower-arm muscles’ movements. To the best of our knowledge, predicting finger motions for these tasks has not been evaluated as part of an end-to-end system and we hope that our method, together with our dataset will be used as a baseline for understanding these motions.

To this end, we present a data-driven approach that allows us to successfully answer our research question. Our key observation, enabling us to successfully solve our inference problem, is that modeling the hand as a robotic manipulator allows to encode an intermediate representation wherein US images are mapped to said configurations. Given a sequence of such learned configurations, coupled with a neural-network architecture that exploits temporal coherence, we are able to infer fine finger motions. We evaluated our method by collecting data from a group of subjects and successfully predicting finger motions in piano-playing and keyboard-typing tasks.

To summarize, the core contributions this paper makes

It is important to state that we do not showcase our results in muscle with any deformation. We performed tests on healthy subjects with fully-functioning hands in order to provide an accurate benchmark for the task we concentrate on.

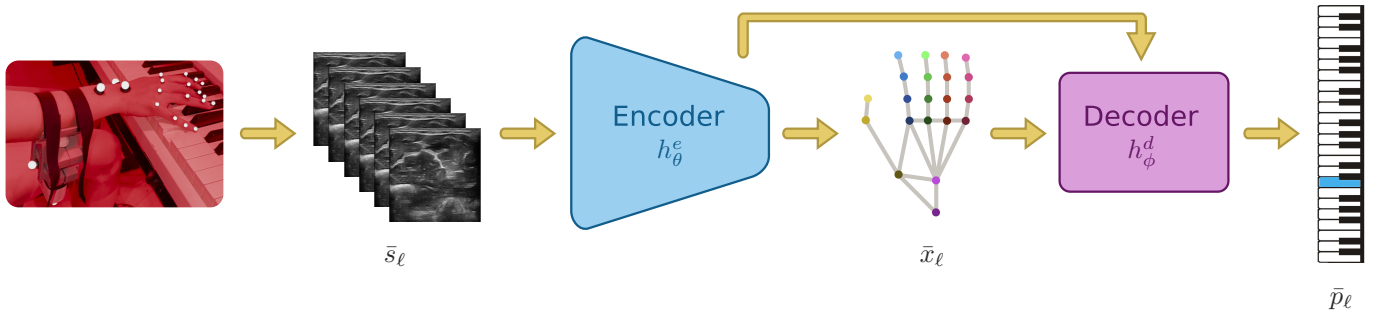


Fig. 1: A schematic flow of the proposed model-based method (sub-section V-B). An ultrasound sensor is placed on the lower arm while the subject is playing the piano. A continuous stream of ultrasound images \bar{s}_ℓ from the sensor is fed into the neural-network encoder h_θ^e which creates a latent representation of hand skeleton configurations \bar{x}_ℓ . The decoder h_ϕ^d receives the latent representation and outputs the vector of probabilities \bar{p}_ℓ indicating the pressed keys. The entire system is trained to produce a common representation for both the skeleton tracking and key prediction tasks.

are (i) presenting a novel learning framework in which the pressing mechanism is motivated by both the dynamics of the muscles and a lower-dimensional representation of the palm of the hand inspired by robotic manipulators; (ii) demonstrating how our framework can be used to replay music played or text typed; and (iii) providing insights into the possibilities of building a robotic device enabling subjects with different morphological muscle structures to perform a wide range of fine finger motions.

II. RELATED WORK

Object grasping is only one of the many actions a human hand performs daily. One of the reasons for the low adoption rates of prosthetic arms among arm amputees is the lack of functionality in performing daily tasks [20]. To detect a larger variance of gestures, advanced wearable surface-EMG (sEMG) sensors have been used (e.g., Myo armband [4, 23]). The array of features provided by this technology allowed researchers to infer more than grasp intention, and classify a varied set of hand gestures using machine-learning (ML) and deep-learning (DL) algorithms [4, 14]. In addition, sEMG was also demonstrated to provide promising performance for arm amputees [23]. It is important to understand that in such a domain, subjects differ in their gestures, which puts forth the requirement of operating across a variety of muscular structures [12].

In recent years, ultrasonic (US) sensing technologies emerged as a promising alternative to EMG. Huang et al. showed that US has the potential to achieve better results compared to EMG [14]. McIntosh et al. proposed to extract the optical flow of an ultrasound stream as a feature prior to the classification phase [19]. Others used ML algorithms demonstrating the feasibility of gesture classification from downsampled US images of the same area [6]. Gesture recognition was achieved with wearable single-transducer sensors [34, 37]. Importantly, these devices differ from medical transducers in that they contain significantly fewer elements and provide coarser views for the lower arm. In addition, researchers demonstrated that similar techniques allow decoupling of

different degrees of freedom and emphasize their dominance in an US image [36]. Unsupervised techniques were also studied, showing discrimination of unlabeled gestures [35], which might imply the possibility to understand muscle behavior of arm amputees without labeling them explicitly. Despite this progress, the feasibility of instructing a robotic hand to deliver fine finger motions is still an open question.

For the analysis of US imagery DL techniques have become increasingly dominant in tasks ranging from tissue segmentation and pathology detection in medical images [33], and image enhancement [30], to replacing traditional beamforming techniques with learned beamformers for faster and better image acquisition [29, 31]. In the context of learning dynamics of human organs, US imaging with transducers placed under the jaw demonstrated reliable speech and pronunciation recreation from imaged tongue movements [2, 15]. Vogt et al. utilized the tongue’s morphological behavior to extrapolate sung pitch and phonemes [32]. Another study investigated the correlation between tongue motion and the frequencies generated by clarinet playing [18]. These previous works suggest that ultrasound provides a rich source of signal describing minute muscular motion.

III. ANATOMICAL BACKGROUND

In this section, we provide the anatomical background required to understand the approach we take to solve our inference problem. Specifically, we explain (in general terms) the relation between lower-arm muscles and the state of the wrist and fingers’ joints. The lower arm contains two main bones, the *ulna* and the *radius*. Surrounding these bones are different muscles that are responsible for the flexion, extension, and rotation of different joints in our palms (including all the fingers). Two annotated US images of this region are presented in Fig. 2, highlighting the muscles relevant to our problem as well as different muscle states corresponding to different finger motions.

We exclude the thumb from the following discussion and concentrate on the remaining four fingers (Index through Little finger). There are three types of joints associated with these

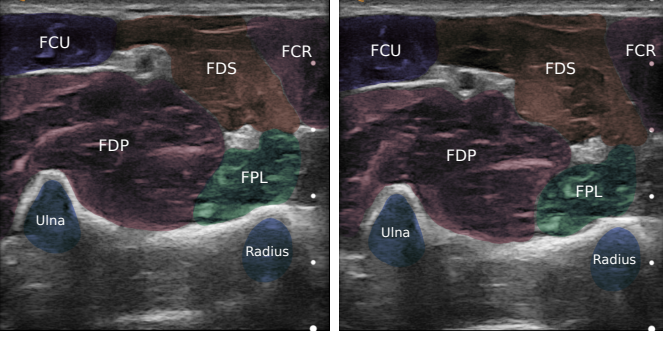


Fig. 2: A visual segmentation of two sampled US images where the top of each image is the skin shell. The Ulna and Radius (the two main bones), are marked in blue, and the flexion muscles are marked with different colors. All fingers are at rest in the left image while on the right image the Ring finger is fully flexed. Notice that the region capturing the FDS muscle in the US image on the right is larger than the one on the left as the FDS muscle becomes more dominant during movement and pushes the other muscles. Figure best viewed in color.

four fingers: the metacarpophalangeal (MP) joints, the proximal interphalangeal (PIP) joints, and the distal interphalangeal (DIP) joints (Fig. 3).

Close to the skin shell, we can find the *flexor carpi radialis* (FCR) and the *flexor carpi ulnaris* (FCU) that are in charge of flexion of the wrist, and the *palmaris longus* (PL) that contributes to flexion for both the wrist and the four fingers, using tendons connecting to the MP joints. The PL is found under the FDS and is not clearly visible given the placement of our US probe but both work in concert actuating some of the joints. Between the FCU and the FCR muscles, we can identify the *flexor digitorum superficialis* (FDS) that flexes the four fingers, and, in full flexion, also contributes to the flexion of the wrist. The FDS connects to tendons that go through the PIP and MP joints of the four fingers. Going deeper into the arm, we find the *flexor digitorum profundus* (FDP). Similar to the FDS, the FDP is in charge of finger flexion and wrist-control assistance using tendons connected to the DIP joints. Close to the FDP, is the *flexor pollicis longus* (FPL), which mainly controls the thumb joints.

To summarize, knowing the state of the FDS and FDP muscles allows (in theory) to estimate the whereabouts of all of the joints of the four fingers by observing US images only. Similarly, the state of the FPL provides us with the knowledge required to understand the movement of the thumb.

IV. PROBLEM DEFINITION AND NOTATION

Following the anatomical background presented in Sec. III we argue that one can infer finger-pressing events in domains such as piano playing or keyboard typing given ultrasound images. However, as we will demonstrate empirically in Sec VI, it is important to consider a *sequence* of ultrasound images that

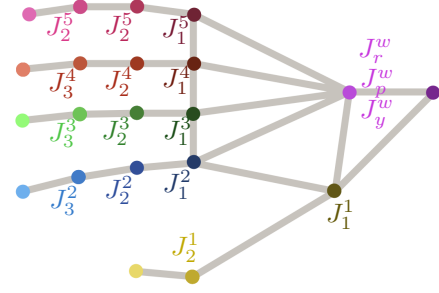


Fig. 3: A visual illustration of the set of joints that form a hand's configuration. The Thumb (F^1) is associated with two joints $[J_1^1, J_2^1]$, the other four fingers F^i ($i \in \{1, \dots, 4\}$) are each associated with three joints $[J_1^i, J_2^i, J_3^i]$ and three additional DOFs are associated with the wrist $[J_r^w, J_p^w, J_y^w]$. The set of joints $\{J_1^i | 1 \leq i \leq 5\}$, $\{J_2^i | 2 \leq i \leq 5\}$ and $\{J_3^i | 2 \leq i \leq 5\}$ correspond to the metacarpophalangeal (MP) joints, the proximal interphalangeal (PIP) joints and the distal interphalangeal (DIP) joints, respectively (see Sec. III).

allows to also exploit the dynamics, improving the learning capabilities. To this end, we assume to be given a sequence of k ultrasound images corresponding to k timestamps and wish to use them to predict which finger was pressed for each of the k timestamps. The rest of this section formalizes this supervised-learning problem.

Let F^1, \dots, F^5 denote the five fingers with F^1 and F^5 corresponding to the Thumb and Little finger, respectively. For each finger F^i and each timestamp t_j we associate a binary variable $p_j^i \in \{0, 1\}$ such that $p_j^i = 1$ if finger F^i is pressed at timestamp t_j and $p_j^i = 0$ otherwise. For every timestamp t_j we denote by $p_j \in \{0, 1\}^5$ the binary vector indicating which fingers are pressed at t_j which we term a *pressing vector*. Namely, $p_j := \langle p_j^1, \dots, p_j^5 \rangle$.

We assume that for every timestamp t_j there is a corresponding ultrasound image s_j as well as a corresponding *configuration* x_j . Here, x_j is an encoding of the fingers and wrists as a set of joint angles (see Fig. 3).

Our training data consists of tuples $\langle \bar{s}_\ell, \bar{x}_\ell, \bar{p}_\ell \rangle$. Here, $\bar{s}_\ell := \langle s_\ell, \dots, s_{k+\ell} \rangle$ is a sequence of k consecutive US images, $\bar{x}_\ell := \langle x_\ell, \dots, x_{k+\ell} \rangle$ is a sequence of k consecutive configurations and $\bar{p}_\ell := \langle p_\ell, \dots, p_{k+\ell} \rangle$ is a sequence of p consecutive pressing vectors all of which start at timestamp t_ℓ . We denote by \mathcal{S} and \mathcal{X} the sets of all sequences of k US images and configurations, respectively.

For each finger F^i and each timestamp t_j we wish to predict p_j^i (i.e., if F^i was pressed at t_j). To this end, our system will output the variable $\hat{p}_j^i \in [0, 1]$ estimating the probability that $p_j^i = 1$. Denote $\hat{p}_j := \langle \hat{p}_j^1, \dots, \hat{p}_j^5 \rangle$ and $\hat{p}_\ell := \langle \hat{p}_\ell, \dots, \hat{p}_{k+\ell} \rangle$.

As we will see, our approach will make use of an intermediate representation corresponding to the configuration at each timestamp. Thus, we will also denote \hat{x}_j the system's estimation of x_j and $\hat{x}_\ell := \langle \hat{x}_\ell, \dots, \hat{x}_{k+\ell} \rangle$.

In Sec. VI we describe the experimental setting which

allows us to obtain the labeled training data for our two representative tasks, piano playing and keyboard typing. In the meantime, we move to describe our approach for solving our inference problem.

V. METHODOLOGY

In this section, we describe our approach to solving the inference problem defined in Sec. IV. We start (Sec. V-A) by describing an approach where we only make use of the US images and the pressing vectors and ignore the corresponding configurations. As we will see in the experimental section (Sec. VI), utilizing the configurations in the training data can lead to better inference capabilities. Thus, in Sec. V-B we extend our first method to account for said configurations. Notice that in this section we concentrate on the high-level learning approach. The specifics of the training and inference procedures are detailed in the experimental section (Sec. VI-C) and the exact network architectures are detailed in the appendix (Sec. A).

A. Learning Finger-pressing Events Directly

To estimate pressing vectors, we use a hybrid architecture starting with a convolutional neural network (CNN) module [8] to extract spatial features from the US images, followed by a recurrent neural network (RNN) [22, 24] to aggregate these features and infer the pressing vectors. Such combination was shown to be effective in various computer-vision tasks that require temporal coherence [9, 17, 40]. By combining these two modules, we create a sequence-to-sequence model, which receives a sequence of US images \bar{s}_ℓ as an input and outputs \hat{p}_ℓ which estimate the pressing vector \bar{p}_ℓ .

We call this the multi-frame (MF) model and denote it as G_θ where θ is the set of model parameters that we optimize in the training phase. This is done by minimizing the negative log-likelihood, i.e.,

$$\mathcal{L}_G(\theta) := -\mathbb{E}_{\bar{s}_\ell \sim \mathcal{S}}[\log P(\hat{p}_\ell | \bar{s}_\ell, \theta)]. \quad (1)$$

B. Learning Finger-pressing Events via Hand Configurations

To estimate pressing vectors while making use of an intermediate representation of the finger's configuration, we use an auto-encoder [1, 22] framework composed of two main blocks—an encoder mapping the sequence of US images \bar{s}_ℓ to a sequence of configurations \hat{x}_ℓ and a decoder using \hat{x}_ℓ to estimate the pressing vector by outputting \hat{p}_ℓ . The encoder's architecture follows the architecture proposed for the MF model (i.e., a CNN followed by an RNN) while the decoder uses an additional RNN module together with a residual connection [10] that feeds the model with the hidden features from the encoder. For a visualization of the inference flow, see Fig 1.

We chose to use an auto-encoder as this architecture was shown to allow a domain expert to inject domain knowledge via an intermediate representation (hand configurations in our setting) [13, 38]. The residual connection was added to better allow the decoder to infer pressing vectors by obtaining knowledge from the US images and the configurations.

We name this model the Configuration-Based Multi-Frame (CBMF) model, and denote it as $H_{\theta, \phi} = h_\phi^d \circ h_\theta^e$ where θ and ϕ are the encoder's and decoder's parameters, respectively which we optimize in the training phase.

While the exact details on how we train this model are explained in the experimental section (Sec. VI-C), we note that the training process is done in two phases. In the first phase, we train only the encoder h_θ^e while in the second phase, we simultaneously train the (pre-trained) encoder h_θ^e together with the (untrained) decoder h_ϕ^d . Splitting the learning into two phases (i.e., to a single and to a multi-modal supervised learning task) was shown to produce better results in similar tasks [26, 27, 39]. Roughly speaking, by pre-training h_θ^e we get a “coarse” mapping between US images \bar{s}_ℓ and predicted finger configurations \hat{x}_ℓ . This allows us to “bootstrap” the network's parameters when solving the entire inference problem in our multi-modal task.

More formally, given \bar{s}_ℓ , \bar{x}_ℓ , and \bar{p}_ℓ , the auto-encoder is trained to predict \bar{x}_ℓ and \bar{p}_ℓ given \bar{s}_ℓ by minimizing the negative log-likelihood of the combination of both terms, i.e.,

$$\mathcal{L}_H(\theta, \phi) = -\mathbb{E}_{\bar{s}_\ell \sim \mathcal{S}, \bar{x}_\ell \sim \mathcal{X}}[\log P(\hat{x}_\ell | \bar{s}_\ell, \theta) + \log P(\hat{p}_\ell | \hat{x}_\ell, \bar{s}_\ell, \phi)]. \quad (2)$$

VI. EXPERIMENTS

In this section, we evaluate our approach for predicting fine finger motions via US images. We start (Sec. VI-A) by describing our experimental setup and continue (Sec. VI-B) to describe our data-collection methodology. We then detail our model architecture and how it was trained (Sec. VI-C) and finish with an analysis of the data collected (Sec. VI-D).

A. Experimental Setup

Our setup includes a Clarius L15HD (wireless B-mode US device), a Roland FP-30 (digital piano), a standard keyboard, and a Vicon motion-capture system. The US's configuration was set for the musculoskeletal task (MSK), with 10 MHz frequency generating a $5 \text{ cm} \times 5 \text{ cm}$ processed image at a rate of 19-21 images per second, in a resolution of 480×480 . It was attached using a wearable strap (as depicted in Fig. 1) to the so-called “transverse” location (see, e.g., McIntosh et al. [19]). The piano and keyboard were used to record the set of pressed notes and keys during each US frame and the Vicon system was used to track the location of the joints of the palm as demonstrated in Fig. 1. Here, the location of each joint (x , y , and z) is captured and used to extract the joint angles that form the hand's configuration, as described in Sec. C of the appendix.

B. Data Collection

We collected data from twelve subjects; averaging at 23 years old, seven of whom are men and five of whom are women. All subjects were confirmed to be right-handed,

Here the superscript ‘e’ and ‘d’ are used to refer to the encoder and decoder modules, respectively.

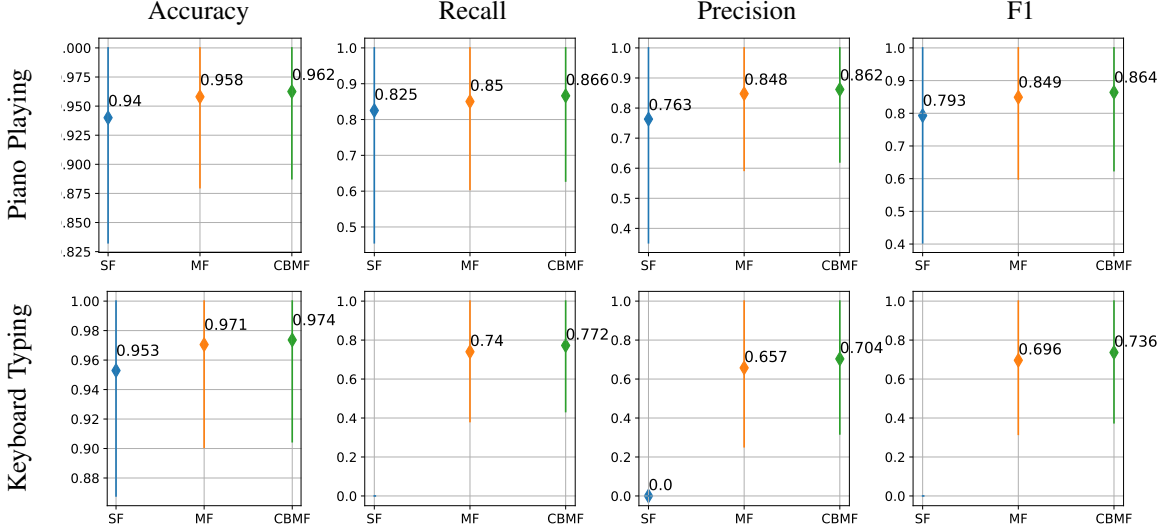


Fig. 4: Evaluation of the MF and CBMF methods (Sec. V) as well as the baseline SF (Sec. VI-D). The first and second rows present evaluation metrics for the piano-playing task, and the keyboard-typing task, respectively. All of the results are after 20 epochs of training and are averaged using the 5-fold validation. Accuracy, recall, precision and F1 were averaged over all test samples on all 5 folds. The rhombus in each interval presents the mean values, while the vertical segment represents the standard deviation range of each metric (clipped at one).

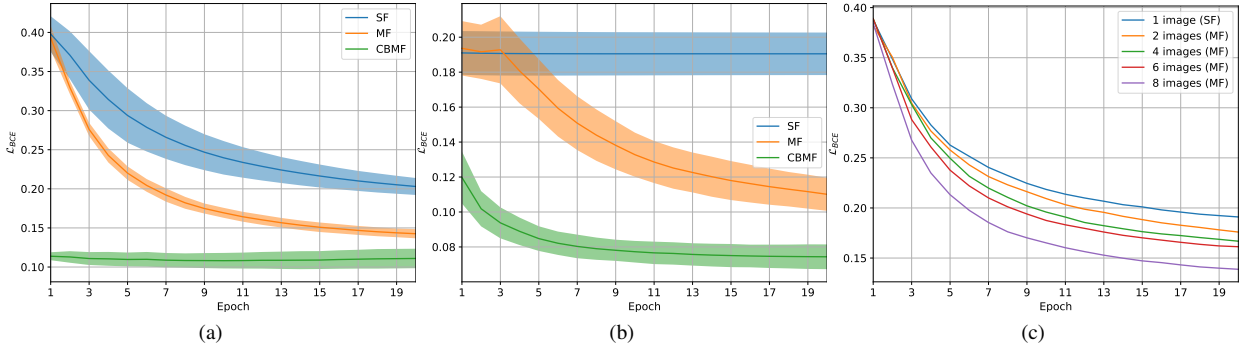


Fig. 5: (a, b) Comparison of the optimization process using \mathcal{L}_{BCE} as a function of the epoch number for the piano-playing and keyboard-typing tasks. (c) Training loss as a function of epoch number for different sizes of US sequences as inputs.

experienced in playing piano, and without any neurological disorders or deformity in the relevant hand area. At the beginning of both tasks, subjects were instructed to put their hands in a stationary state in which each of their fingers must be on the same note/key for the entire session.

For piano playing, subjects were asked to play melodies that only require five distinguished notes and can be played using one hand only. For keyboard typing, subjects were asked to randomly type on each of the five keys their fingers are stationed over, while not using more than one key at the same time. For each task, subjects were asked to perform 2-3 sessions, with approximately ninety seconds for each session, and rest between sessions. The process was approved by the institution’s Ethics Committee. The final dataset includes 44, 596 samples for piano playing and 42, 143 samples for keyboard typing, each sample representing the tuple $\langle \bar{s}_\ell, \bar{x}_\ell, \bar{p}_\ell \rangle$ defined

in Sec. IV.

C. Model Training

Before training, both images s_i and configurations x_i were normalized to the range of $[0, 1]$. On feedforward, our MF model G_θ receive a sequence of $k = 8$ US images \bar{s}_ℓ , such that each image s_i is downsampled to a resolution of 224×224 and fed to the CNN block to extract feature maps. These feature maps are then flattened and concatenated into a temporal features vector that is used as the input for the RNN module, to output k pressing vectors. Our CBMF model $H_{\theta, \phi}$ works such that the encoder h_θ^e is being fed with the images similar to the MF model, and output k configurations, that are then fed to the decoder h_ϕ^d (additional RNN block), along with the features from the residual connection, in the same way that the extracted feature maps are being fed. The decoder h_ϕ^d

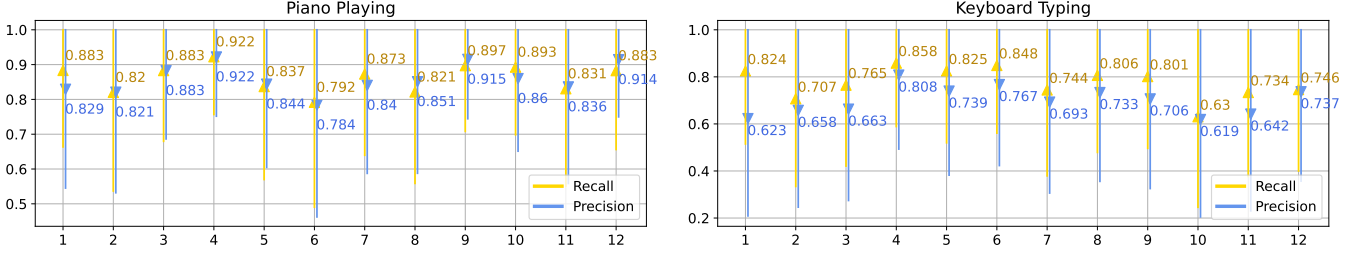


Fig. 6: Recall and precision for the CBF model on the piano-playing and keyboard-typing tasks (left and right images, respectively) for each of the twelve subjects. Vertical segments denote one standard deviation.

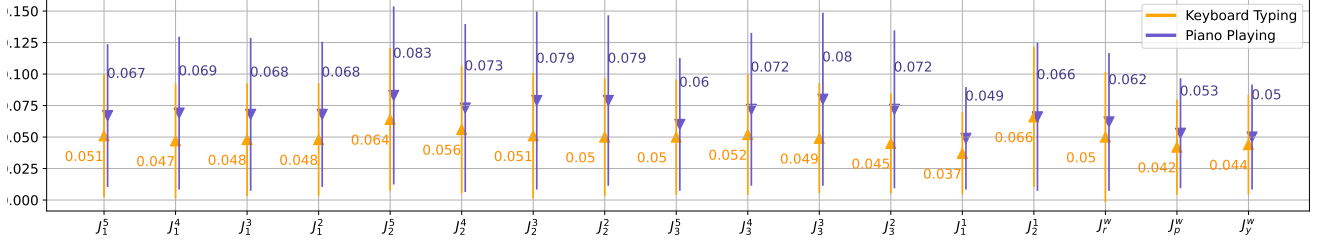


Fig. 7: Error values in radians for joint angles using our CBF model to predict hand configurations, on both tasks.

is designed to output k predicted configurations. The entire architecture is detailed in Sec. A of the appendix.

On back propagation, for the predicted configurations, the applied loss function for $N = 32$ samples in a batch is the Mean Squared Error (MSE) on all configurations, i.e.,

$$\mathcal{L}_{MSE} = \frac{1}{N \cdot k} \sum_{i \in N \cdot k} \|\hat{x}_i - x_i\|_2^2.$$

A configuration x_i is a vector of 17 angles—3 for each finger excluding the thumb, 2 for the thumb, and 3 for the wrist, as depicted in Fig. 3. For the predicted pressing vectors, the applied loss objective for $N = 32$ samples in a batch, such that each sample is k vectors of $M = 5$ probabilities, is the Binary Cross Entropy (BCE) for all probabilities, i.e.,

$$\mathcal{L}_{BCE} = \frac{1}{N \cdot k \cdot M} \sum_{i \in M} \sum_{j \in N \cdot k} p_j^i \log \hat{p}_j^i + (1 - p_j^i) \log(1 - \hat{p}_j^i).$$

To train the MF model, we apply the loss function \mathcal{L}_{BCE} , and to train the CBF model, we apply the combined loss function $\lambda \mathcal{L}_{MSE} + \mathcal{L}_{BCE}$, where λ is chosen using a trial-and-error procedure, as described in Sec. B of the appendix. All training sessions were executed for 20 epochs, to avoid overfitting. For the optimization method, Adam [16] was used for all tasks, with a learning rate of 0.001.

D. Results

In all of the experiments, we evaluated all methods using 5-fold validation: for each task, all sessions of all subjects were divided into five folds, and trained such that the i 'th fold was set aside for testing and not used in training. This ensures that the test set contains unseen intervals of motions.

How good are the proposed methods? We start by evaluating the inference capabilities of our two models (MF and

CBMF) on the piano-playing task and keyboard-typing task by plotting the accuracy, recall, precision and $F1$ (Fig. 4) as well as the different model loss as training progresses (Fig. 5). As a baseline, we added a simple model where we take our MF module and replace the RNN with a multilayer perceptron (MLP) to predict a single pressing vector. On inference, the model receives a single 224×224 image. On evaluation, this model is evaluated using the same 5-fold validation over the same datasets. We call this the single-frame (SF) model.

Notice that the overall performance for piano playing is significantly higher than for keyboard typing. We associate this difference with differences in pressing durations and body postures between the two tasks: The maximum offset that a note can offer by our piano is 10.45 mm, while the maximum offset for a key from our keyboard is 2.95 mm. This implies longer flexing of the subjects when playing the piano, which leads to more dominant motions in US images. Additionally, the character of movements of the hand while playing the piano naturally involves different body postures which often leads to different wrist angles. This, in turn, also leads to more dominant motions in US images.

Moving on to comparing the different models, the SF model is unable to recreate the finer task of keyboard typing, but is able to learn to play the piano. This backs up our conjecture that multiple consecutive frames are required to infer fine finger motions. Notice that the MF model outperforms the SF model while the CBF model outperforms both. This is especially noticeable in the harder keyboard-typing task which backs up our conjecture that an intermediate configuration-based representation allows to better infer fine finger motions. Note that the different metrics, such as recall and precision, were averaged over the entire sequence in each sample. This, again, backs up our conjecture that sharing the knowledge

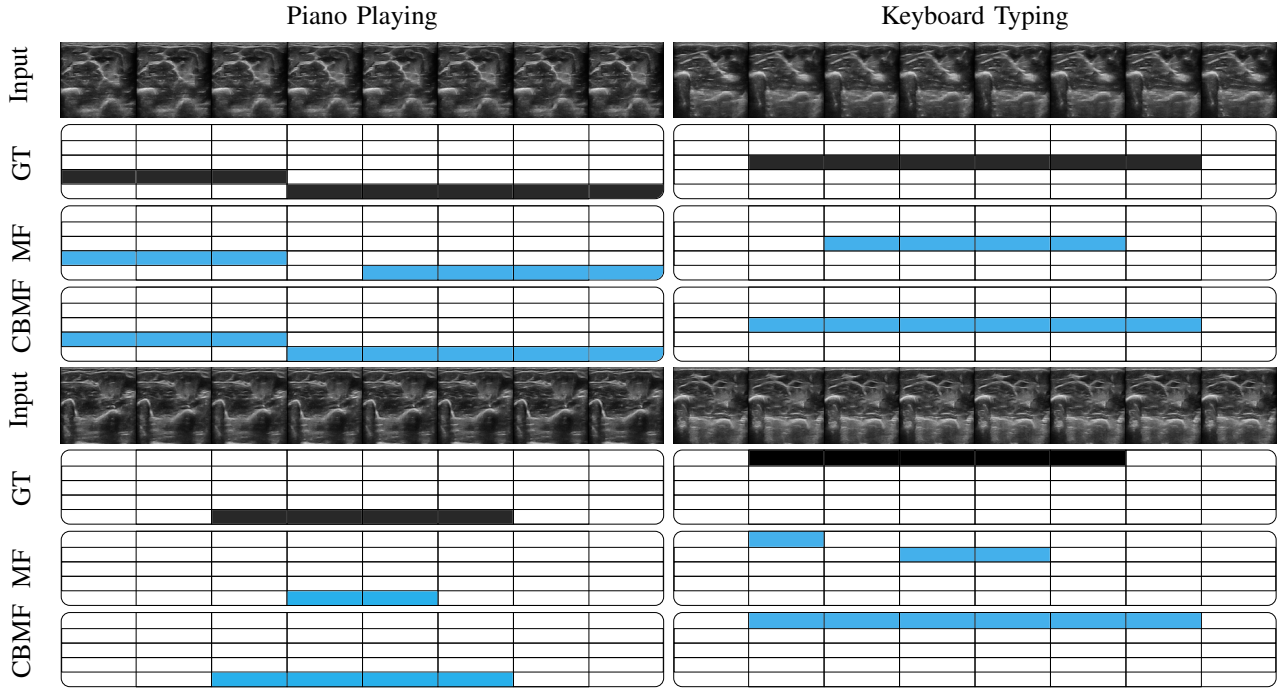


Fig. 8: Samples from executing the MF and CBMF models for both tasks. In each rollout, the upper row represents finger F^5 (Little finger) and the lower row represents finger F^1 (Thumb). Ground-truth (GT) labels are marked in black. The differences between both models are expressed in consistency and number of false-positive predictions. Notice from the US images how hard is it for a human eye to understand subtle morphological changes during such gentle movements.

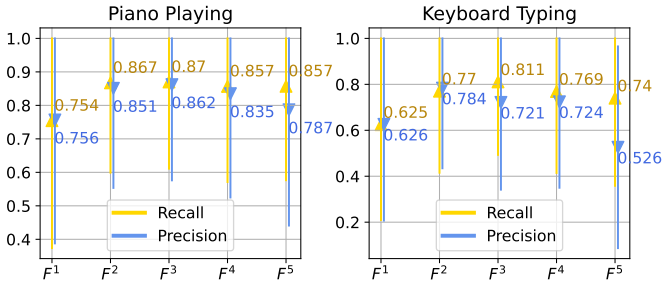


Fig. 9: Recall and precision separated for all five fingers. Vertical segments denote one.

between subsequent images improves results. For a representative visualization of the difference between the MF and CBMF models on the two tasks, see Fig. 8

We also tested both tasks on additional common computer-vision models, such as the VGG16 [25] model (pretrained on ImageNet [5] and not pretrained), and C3D [28], which were shown to perform favorably in video classification. However, the models did not converge in any of the tasks and therefore were excluded from evaluation. Importantly, our method works without any preprocessing steps that require recording data before the inference procedure. I.e., we can work in an online setting. This is in contrast to existing methods for which subjects were instructed to perform gestures according to predefined instructions [6], or separate between gestures categories before feature extraction [19].

How feasible is the method for a group of subjects? We plot the different metrics for each subject individually to see how the CBMF model varies across different subjects (Fig. 6). Evidently, the better the model is in understanding a subject's movements, the smaller the error margin is. Furthermore, for all subjects except #8, the results for piano playing are better than for keyboard typing. Finally, we observe that there is a correlation between those who performed better on keyboard typing, to those who performed better on piano playing, which concludes the discussion on the importance of subjects' muscles structure in solving such tasks.

How important is the size of the sequence for the learning procedure? To understand the importance of the duration of the sequence of US images, we tested the MF on sequences of size $k \in \{2, 4, 6, 8\}$. For $k = 1$, we used the SF model (Fig. 5). Indeed, convergence on the test set improves gradually the more we increase the sequence size k .

How well does the system works for all fingers? We computed the recall and precision values for each of the fingers individually to understand how each of the fingers affects the quality of the solution (Fig. 9). On both tasks, the model performs better on fingers F^2, F^3 and F^4 , rather than on fingers F^1 and F^5 . A possible explanation is that this is due to the fact that operating the three middle fingers causes larger movement in the flexion muscles that are found in the US images when compared to the Thumb and Little finger. As

We did not use a sequence of more than 8 US images due to GPU memory limitations. We assume that larger sequences could have improved the results even better.

illustrated in Fig 2, the muscle that is responsible for the movement of the Thumb is significantly less dominant than the rest of the muscles, which might explain why Thumb movement is the least-understandable gesture.

How accurate are the estimated configurations? We evaluated the error values (in radians) of our CBMF model for each of the individual 17 joints in a configuration (see Fig. 3). Results, depicted in Fig. 7, demonstrate that the more the task requires longer movements, the higher the error margin, especially for the more dominant joints, such as fingers F^2 and F^3 . Interestingly, the DOFs that are more dominant near the wrist ($J_1^1, J_r^w, J_p^w, J_y^w$), achieve a smaller error on average, which might relate to the high region captured by the relative muscles in the US images.

VII. DISCUSSION AND FUTURE WORK

In this paper, we explored the task of predicting and differentiating between fine finger motions by only having access to a stream of US images of the lower-arm muscles. We show that incorporating temporal coherence and a kinematic representation of the hand into data-driven methods are essential for solving tasks that require an understanding of continuous gentle motions of muscles.

We believe that the inference capabilities we present which allow us to precisely mimic human hand motions pave the way towards enabling fully-operational prostheses for those in need. We now continue to present directions that can be used to reach our ultimate goal.

A. Restoring Motions For Different Conditions

We would like to be able to reconstruct motions for people with different deformations or conditions, such as different types of amputations, where accurate labels of motions are unavailable for use. Thus, requiring us to search for data-driven solutions that can use the knowledge inferred from able-bodied subjects, to recreate unlabeled motions in unsupervised cases. We believe that combining methods acquired in this work, together with unsupervised techniques to infer unknown motions, can create a huge step towards biomedical solutions for people in need.

B. Generalization For Unknown Subjects

The task of recreating accurate motions for a person that was not examined during recording is what we see as one of the next stages in understanding hand motions. When using US, we saw that the morphological differences between different subjects are deeper than the differences between the movements themselves. In such conditions, data-driven approaches will need more information regarding the person in order to allow understanding of an unseen muscle's structure. In the future, we seek to require a deeper understanding of the differences between different people with different muscle's structure.

C. Multi-task Prediction for Hand Motions

We seek to exploit better opportunities by adopting the unique modality of hand configuration, and using it for other tasks. We see in this the potential to create a multi-task method that can thoroughly understand not only the motions, but also infer the task from the motions, and create a solution that can provide a wider range of features. Importantly, currently available robotic prostheses are commonly equipped with manual options to change states, due to the inability to understand more than a single task, a reality we wish to change.

ACKNOWLEDGMENTS

This project has received funding from the European Research Council (ERC) under the European Union's Horizon 2020 research and innovation programme (grant agreement No. 863839). We also thank Haifa3D, a non-profit organization providing self-made 3d-printed solutions, for their consulting and support through the research.

APPENDIX

A. Network Architecture

Tables I and Table II shows the network architectures for the MF and CBMF models respectively. The tables are divided into blocks, such that the first block represents the CNN module and the others represent the RNN modules. The input shape for both models is $[224 \times 224 \times 8]$, and corresponding to 8 consecutive grayscale ultrasound images. The shape of the intermediate representation is $[8 \times 17]$, corresponding to a trajectory of 8 robotic configurations, each of size 17. The output shape is $[5 \times 8]$, denoting a consecutive set of 8 vectors of probabilities, each containing 5 probabilities, denoting 5 fingers.

The CNN module is based on the encoding part of UNet [21], due to the high reputation of this architecture among medical imaging tasks. This block is used to extract $512 \ 3 \times 3$ feature maps from each of the 8 images, such that the same parameters are shared across all images. These are flattened, concatenated, and fed into the recurrent block. In the CBMF model, The trajectory, along with 8×128 features are taken from the output of the second GRU layer, concatenated, and fed as an input to the decoder.

B. Losses Weighting

We empirically chose the value of λ to minimize the objective function $\lambda \mathcal{L}_{MSE} + \mathcal{L}_{BCE}$. Here, we executed training sessions to see the results for $\lambda \in \{2^i | i \in [0, \dots, 6]\}$ and chose the result yielding the lowest \mathcal{L}_{BCE} , without harming the optimization of the \mathcal{L}_{MSE} . Results, presented in Fig. 10, show that by taking $\lambda = 4$, we benefit from using both modalities. The same experiment with $\lambda = 0$ (only \mathcal{L}_{BCE}) resulted in $\mathcal{L}_{BCE} = 0.093$ and $\mathcal{L}_{MSE} = 2.582$, and therefore was ruled out from the evaluation.

Layer	Act.	Out. shape	Parameters
Conv2D	ReLU	$224 \times 224 \times 32$	320
Conv2D	ReLU	$224 \times 224 \times 32$	9,248
MaxPooling2D (2 × 2)	-	$112 \times 112 \times 32$	-
Conv2D	ReLU	$112 \times 112 \times 64$	18.50k
Conv2D	ReLU	$112 \times 112 \times 64$	36.93k
MaxPooling2D (2 × 2)	-	$56 \times 56 \times 64$	-
Conv2D	ReLU	$56 \times 56 \times 128$	73.86k
Conv2D	ReLU	$56 \times 56 \times 128$	147.58k
MaxPooling2D (2 × 2)	-	$28 \times 28 \times 128$	-
Conv2D	ReLU	$28 \times 28 \times 256$	295.17k
Conv2D	ReLU	$28 \times 28 \times 256$	590.08k
Dropout (p=0.3)	-	$28 \times 28 \times 256$	-
MaxPooling2D (2 × 2)	-	$14 \times 14 \times 256$	-
Conv2D	ReLU	$14 \times 14 \times 512$	1.18M
Conv2D	ReLU	$14 \times 14 \times 512$	2.36M
Dropout (p=0.3)	-	$14 \times 14 \times 512$	-
MaxPooling2D (4 × 4)	-	$3 \times 3 \times 512$	-
Flatten	-	4608	-
<hr/>			
Concatenate (8 images)	-	8×4608	-
GRU	ReLU	8×1024	17.31M
GRU	ReLU	8×128	443.14K
GRU	Linear	8×5	2,025
Total			22.93M

TABLE I: Neural-network architecture of our MF model G_θ .

Layer	Act.	Out. shape	Parameters
Conv2D	ReLU	$224 \times 224 \times 32$	320
Conv2D	ReLU	$224 \times 224 \times 32$	9,248
MaxPooling2D (2 × 2)	-	$112 \times 112 \times 32$	-
Conv2D	ReLU	$112 \times 112 \times 64$	18.50k
Conv2D	ReLU	$112 \times 112 \times 64$	36.93k
MaxPooling2D (2 × 2)	-	$56 \times 56 \times 64$	-
Conv2D	ReLU	$56 \times 56 \times 128$	73.86k
Conv2D	ReLU	$56 \times 56 \times 128$	147.58k
MaxPooling2D (2 × 2)	-	$28 \times 28 \times 128$	-
Conv2D	ReLU	$28 \times 28 \times 256$	295.17k
Conv2D	ReLU	$28 \times 28 \times 256$	590.08k
Dropout (p=0.3)	-	$28 \times 28 \times 256$	-
MaxPooling2D (2 × 2)	-	$14 \times 14 \times 256$	-
Conv2D	ReLU	$14 \times 14 \times 512$	1.18M
Conv2D	ReLU	$14 \times 14 \times 512$	2.36M
Dropout (p=0.3)	-	$14 \times 14 \times 512$	-
MaxPooling2D (4 × 4)	-	$3 \times 3 \times 512$	-
Flatten	-	4608	-
<hr/>			
Concatenate (8 images)	-	8×4608	-
GRU	ReLU	8×1024	17.31M
GRU	ReLU	8×128	443.14K
GRU	Linear	8×17	7,497
<hr/>			
Merge	-	8×145	-
GRU	ReLU	8×256	309.50K
GRU	ReLU	8×128	148.22K
GRU	Linear	8×5	2,025
Total			22.93M

TABLE II: Neural-network architecture of our CBMF model $H_{\theta, \phi}$.

C. Joints Computation

The set of joint angles forming the configuration space is acquired by placing markers on the relevant joints and using a motion-capture system to obtain the location $[x, y, z]$ of each marker. Then, the angle of each joint is acquired by computing

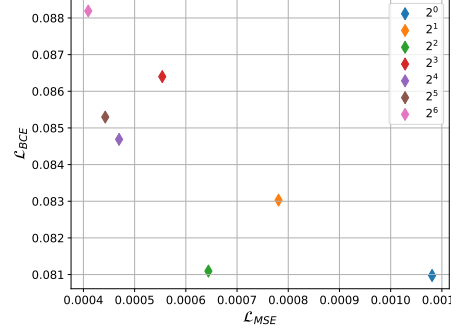


Fig. 10: \mathcal{L}_{BCE} and \mathcal{L}_{MSE} for different values of λ . On average, results are showing that using lower values of λ yields lower values of \mathcal{L}_{BCE} and higher values of λ yields lower values of \mathcal{L}_{MSE} and higher values of \mathcal{L}_{BCE} .

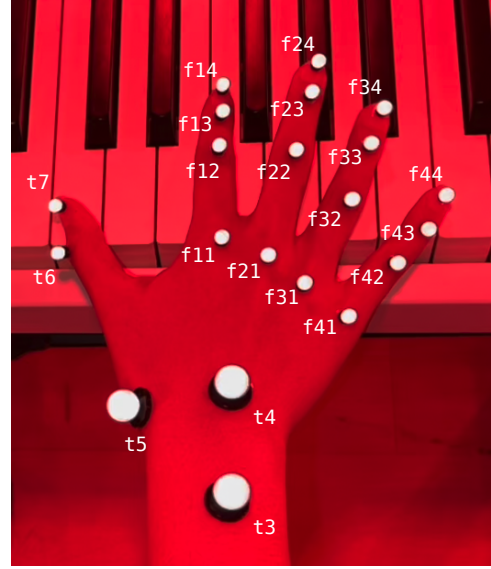


Fig. 11: An image showing the position of each marker on the subject's hand. The label alongside each marker represents the 3D position of the marker in the environment.

the angle between the two related vectors from the markers' locations. To explain it, we first denote the vector between two points as the subtraction between the vectors of the two points. For example, given two 3D points (that can be related as two 3D vectors w.r.t. some reference frame) f_{42} and f_{43} , we denote the vector from f_{42} to f_{43} using the following:

$$\vec{v}_{f_{42} \rightarrow f_{43}} = \vec{f}_{43} - \vec{f}_{42}. \quad (3)$$

Next, we compute the angle between two vectors. For example, by having the vector f_{42} to f_{43} and the vector from f_{42} to f_{41} , we compute the joint angle J_2^5 using the following:

$$J_2^5 = \arctan2(\|\vec{v}_{f_{42} \rightarrow f_{41}} \times \vec{v}_{f_{42} \rightarrow f_{43}}\|_2, \vec{v}_{f_{42} \rightarrow f_{41}} \cdot \vec{v}_{f_{42} \rightarrow f_{43}}). \quad (4)$$

Then, we can define the computed joints for each of the

four fingers F^2, \dots, F^5 . We will use finger F^5 (Little finger) for example. The three joints that are required to illustrate the movements are J_1^5 , J_2^5 and J_3^5 . Hence, we will compute J_1^5 and J_3^5 using:

$$\begin{aligned} J_1^5 &= \arctan2(\|\vec{v}_{f_{41} \rightarrow t_5} \times \vec{v}_{f_{41} \rightarrow f_{42}}\|_2, \\ &\quad \vec{v}_{f_{41} \rightarrow t_5} \cdot \vec{v}_{f_{41} \rightarrow f_{42}}), \\ J_3^5 &= \arctan2(\|\vec{v}_{f_{42} \rightarrow f_{41}} \times \vec{v}_{f_{42} \rightarrow f_{43}}\|_2, \\ &\quad \vec{v}_{f_{42} \rightarrow f_{41}} \cdot \vec{v}_{f_{42} \rightarrow f_{43}}). \end{aligned} \quad (5)$$

Similarly, fingers F^1 , F^2 , and F^3 are calculated in the same way. As for the Thumb, we compute two joints; J_1^1 and J_2^1 similar to Eq. 5:

$$\begin{aligned} J_2^1 &= \arctan2(\|\vec{v}_{t_6 \rightarrow t_7} \times \vec{v}_{t_6 \rightarrow t_5}\|_2, \\ &\quad \vec{v}_{t_6 \rightarrow t_7} \cdot \vec{v}_{t_6 \rightarrow t_5}), \end{aligned} \quad (6)$$

where the joint J_1^1 is acquired by computing the angle between $\vec{v}_{t_5 \rightarrow t_6}$ and the normal vector to the plane approximating the palm's plane, by taking the three points f_{11} , f_{41} and t_4 . Denoting this normal as \hat{n}_p , joint J_1^1 is computed using:

$$\begin{aligned} J_1^1 &= \arctan2(\|\vec{v}_{t_5 \rightarrow t_6} \times \hat{n}_p\|_2, \\ &\quad \vec{v}_{t_5 \rightarrow t_6} \cdot \hat{n}_p). \end{aligned} \quad (7)$$

This is done differently in order to take the angle that is related to the pressing motion of the Thumb. As for the 3 DOFs of the wrist, we have J_r^w , J_p^w , and J_y^w for roll, pitch and yaw respectively. As for pitch, we compute the angle between \hat{n}_p and $\vec{v}_{t_4 \rightarrow t_3}$. For yaw, we compute the angle between $\vec{v}_{f_{41} \rightarrow f_{11}}$ and $\vec{v}_{t_4 \rightarrow t_3}$, and for roll, we compute the angle between \hat{n}_p and a vector denoted from two additional points that are located on the elbow.

REFERENCES

- [1] P. Baldi. Autoencoders, unsupervised learning, and deep architectures. In *ICML*, volume 27, pages 37–50, 2012.
- [2] H. Bliss, S. Bird, A. P. Cooper, S. Burton, and B. Gick. Seeing speech: Ultrasound-based multimedia resources for pronunciation learning in indigenous languages. 2018.
- [3] C. Connolly. Prosthetic hands from touch bionics. *Ind. Rob.*, 2008.
- [4] U. Côté-Allard, C. L. Fall, A. Drouin, A. Campeau-Lecours, C. Gosselin, K. Glette, F. Laviolette, and Benoit Gosselin. Deep learning for electromyographic hand gesture signal classification by leveraging transfer learning. *arXiv*, abs/1801.07756, 2018.
- [5] J. Deng, W. Dong, R. Socher, L. Li, K. Li, and L. Fei-Fei. Imagenet: A large-scale hierarchical image database. In *CVPR*, pages 248–255, 2009.
- [6] A. S. Dhawan, B. Mukherjee, S. Patwardhan, N. Akhlaghi, G. Levay, R. Holley, W. M. Joiner, M. Harris-Love, and S. Sikdar. Proprioceptive sonomyographic control: A novel method of intuitive proportional control of multiple degrees of freedom for upper-extremity amputees. *arXiv*, abs/1808.06543, 2018.
- [7] J. A. George, T. S. Davis, M. R. Brinton, and G. A. Clark. Intuitive neuromyoelectric control of a dexterous bionic arm using a modified kalman filter. *arXiv*, abs/1908.10522, 2019.
- [8] J. Gu, Z. Wang, J. Kuen, L. Ma, A. Shahroudy, B. Shuai, T. Liu, X. Wang, and G. Wang. Recent advances in convolutional neural networks. *arXiv*, abs/1512.07108, 2015.
- [9] J. Guo, Y. Liu, Q. Yang, Y. Wang, and S. Fang. Gps-based citywide traffic congestion forecasting using cnn-rnn and c3d hybrid model. *Transportmetrica A*, 17(2): 190–211, 2021.
- [10] K. He, X. Zhang, S. Ren, and J. Sun. Deep residual learning for image recognition. In *CVPR*, pages 770–778, 2016.
- [11] P. Herberts. Myoelectric signals in control of prostheses: Studies on arm amputees and normal individuals. *Acta. Orthop.*, 40(sup124):1–83, 1969.
- [12] Y. Herbst, L. Zelnik-Manor, and A. Wolf. Analysis of subject specific grasping patterns. *PLoS One*, 15(7): e0234969, 2020.
- [13] J. Hu, X. Guo, J. Chen, G. Liang, F. Deng, and T. L. Lam. A two-stage unsupervised approach for low light image enhancement. *IEEE Robotics Autom. Lett.*, 6(4): 8363–8370, 2021.
- [14] Y. Huang and H. Liu. Performances of surface EMG and ultrasound signals in recognizing finger motion. In *HSI*, pages 117–122, 2016.
- [15] N. Kimura, M. Kono, and J. Rekimoto. Sottovoce: An ultrasound imaging-based silent speech interaction using deep neural networks. In *CHI*, page 146, 2019.
- [16] D. P. Kingma and J. Ba. Adam: A method for stochastic optimization. In *ICLR*, 2015.
- [17] W. Lu, J. Li, Y. Li, A. Sun, and J. Wang. A cnn-lstm-based model to forecast stock prices. *Complex.*, 2020: 6622927:1–6622927:10, 2020.
- [18] S. M. Lulich, S. Charles, and B. Lulich. The relation between tongue shape and pitch in clarinet playing using ultrasound measurements. *J. Acoust. Soc. Am.*, 141(3): 1759–1768, 2017.
- [19] J. McIntosh, A. Marzo, M. Fraser, and C. Phillips. Echoflex: Hand gesture recognition using ultrasound imaging. In *CHI*, pages 1923–1934, 2017.
- [20] L. Resnik, M. R. Meucci, S. Lieberman-Klinger, C. Fantini, D. L. Kelty, R. Disla, and N. Sasson. Advanced upper limb prosthetic devices: implications for upper limb prosthetic rehabilitation. *Arch. Phys. Med. Rehabil.*, 93(4):710–717, 2012.
- [21] O. Ronneberger, P. Fischer, and T. Brox. U-net: Convolutional networks for biomedical image segmentation. In *MICCAI*, volume 9351, pages 234–241, 2015.
- [22] D. E. Rumelhart, G. E. Hinton, and R. J. Williams. Learning internal representations by error propagation. Technical report, 1985.

- [23] S. Said, M. Sheikh, F. Al-Rashidi, Y. Lakys, T. Beyrouthy, A. Nait-ali, et al. A customizable wearable robust 3d printed bionic arm: Muscle controlled. In *BioSMART*, pages 1–6, 2019.
- [24] A. Sherstinsky. Fundamentals of recurrent neural network (RNN) and long short-term memory (LSTM) network. *arXiv*, abs/1808.03314, 2018.
- [25] Karen Simonyan and Andrew Zisserman. Very deep convolutional networks for large-scale image recognition. In *ICLR*, 2015.
- [26] A. Singh, H. Liu, G. Zhou, A. Yu, N. Rhinehart, and S. Levine. Parrot: Data-driven behavioral priors for reinforcement learning. In *ICLR*, 2021.
- [27] C. Tan, F. Sun, B. Fang, T. Kong, and W. Zhang. Autoencoder-based transfer learning in brain–computer interface for rehabilitation robot. *Int. J. Adv. Robot. Syst.*, 16(2), 2019.
- [28] D. Tran, L. D. Bourdev, R. Fergus, L. Torresani, and M. Paluri. Learning spatiotemporal features with 3d convolutional networks. In *ICCV*, pages 4489–4497, 2015.
- [29] R. J. G. van Sloun, R. Cohen, and Y. C. Eldar. Deep learning in ultrasound imaging. *arXiv*, abs/1907.02994, 2019.
- [30] S. Vedula, O. Senouf, A. M. Bronstein, O. V. Michailovich, and M. Zibulevsky. Towards ct-quality ultrasound imaging using deep learning. *arXiv*, abs/1710.06304, 2017.
- [31] S. Vedula, O. Senouf, G. Zurakhov, A. M. Bronstein, O. V. Michailovich, and M. Zibulevsky. Learning beam-forming in ultrasound imaging. In *MIDL*, volume 102, pages 493–511, 2019.
- [32] F. Vogt, G. McCaig, M. A. Ali, and S. S. Fels. Tongue ‘n’ groove: An ultrasound based music controller. In *NIME*, pages 60–64, 2002.
- [33] Y. Wang, X. Ge, H. Ma, S. Qi, G. Zhang, and Y. Yao. Deep learning in medical ultrasound image analysis: A review. *IEEE Access*, 9:54310–54324, 2021.
- [34] J. Yan, X. Yang, X. Sun, Z. Chen, and H. Liu. A lightweight ultrasound probe for wearable human–machine interfaces. *IEEE Sens. J.*, 19(14):5895–5903, 2019.
- [35] X. Yang, D. Zhou, Y. Zhou, Y. Huang, and H. Liu. Towards zero re-training for long-term hand gesture recognition via ultrasound sensing. *IEEE J. Biomed. Health Informatics*, 23(4):1639–1646, 2019.
- [36] X. Yang, J. Yan, Y. Fang, D. Zhou, and H. Liu. Simultaneous prediction of wrist/hand motion via wearable ultrasound sensing. *IEEE Trans. Neural Syst. Rehabilitation Eng.*, 28(4):970–977, 2020.
- [37] X. Yang, Z. Chen, N. Hettiarachchi, J. Yan, and H. Liu. A wearable ultrasound system for sensing muscular morphological deformations. *IEEE Trans. Syst. Man Cybern. Syst.*, 51(6):3370–3379, 2021.
- [38] Y. Yang, B. Li, P. Li, and Q. Liu. A two-stage clustering based 3d visual saliency model for dynamic scenarios. *IEEE Trans. Multim.*, 21(4):809–820, 2019.
- [39] D. Zadok, D. McDuff, and A. Kapoor. Modeling affect-based intrinsic rewards for exploration and learning. In *ICRA*, pages 13078–13084, 2021.
- [40] Q. Zou, H. Jiang, Q. Dai, Y. Yue, L. Chen, and Q. Wang. Robust lane detection from continuous driving scenes using deep neural networks. *IEEE Trans. Veh. Technol.*, 69(1):41–54, 2020.